

AWaRe-SAC: Proactive Slice Admission Control under Weather-Induced Capacity Uncertainty

Dror Jacoby*, Yanzhi Li*, Shuyue Yu, Nicola Di Cicco, Hagit Messer, Gil Zussman, and Igor Kadota

Abstract—As emerging applications demand higher throughput and lower latencies, operators are increasingly deploying millimeter-wave (mmWave) links within x-haul transport networks, spanning fronthaul, midhaul, and backhaul segments. However, the inherent susceptibility of mmWave frequencies to weather-related attenuation, particularly rain fading, complicates the maintenance of stringent Quality of Service (QoS) requirements. This creates a critical challenge: making admission decisions under uncertainty regarding future network capacity. To address this, we develop a proactive slice admission control framework for mmWave x-haul networks subject to rain-induced fluctuations. Our objective is to improve network performance, ensure QoS, and optimize revenue, thereby surpassing the limitations of standard reactive approaches. The proposed framework integrates a deep learning predictor of future network conditions with a proactive Q-learning-based slice admission control mechanism. We validate our solution using real-world data from a mmWave x-haul deployment in a dense urban area, incorporating realistic models of link capacity attenuation and dynamic slice demands. Extensive evaluations demonstrate that our proactive solution achieves 2–3x higher long-term average revenue under dynamic link conditions, providing a scalable and resilient framework for adaptive admission control.

Index Terms—Network slicing, proactive admission control, mmWave, resource uncertainty, weather-induced attenuation

I. INTRODUCTION

mmWave frequencies, particularly within the high V-band around 70 GHz, play a crucial role in enabling next-generation 5G and envisioned 6G networks to meet stringent data-rate and latency demands [1]. However, these frequencies are highly susceptible to environmental factors such as rain, leading to significant signal degradation, and reduced reliability [2]–[4]. This prominent degradation enables rainfall monitoring using communication links [4], [5], a practical application of the Integrated Sensing and Communication (ISAC) paradigm [6]. From a network perspective, satisfying stringent QoS requirements of dynamic traffic demands under time-varying link capacities create complex challenges for operators, driving the need for resilient, adaptive strategies to mitigate communication disruptions and optimize network performance.

Most prior research (discussed in Sec. II) on slice admission control has focused on reactive algorithms, often considering networks with constant (and known) link capacities. These prior works typically overlook weather-induced fluctuations

Dror Jacoby and Hagit Messer are with the School of Electrical Engineering, Tel Aviv University. Yanzhi Li and Igor Kadota are with the Department of Electrical and Computer Engineering, Northwestern University. Shuyue Yu and Gil Zussman are with the Department of Electrical Engineering, Columbia University. Nicola Di Cicco is with the Department of Electronics, Information and Bioengineering, Politecnico di Milano. *These authors contributed equally to this work.

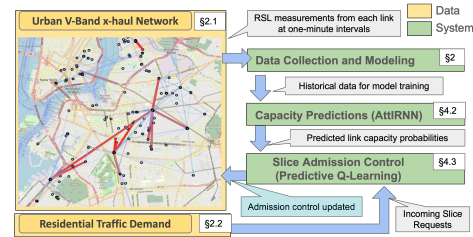


Fig. 1: Overview of the AWaRe-SAC framework workflow.

that can significantly degrade mmWave links. **To the best of our knowledge, our framework is the first to integrate weather-aware capacity forecasting and slice admission in mmWave backhaul.**

We develop an Adaptive Weather-aware Real-time Slice Admission Control (AWaRe-SAC) framework that tightly integrates: (i) **Prediction phase** which leverages historical link measurements to forecast short-term link attenuation (in the next few minutes), also capturing prediction uncertainty. (ii) **Slice admission control phase** which incorporates sequences of predictions (and their uncertainty) to proactively overcome reductions in capacity, fulfill demand requests, and optimize the allocation of slicing resources.

Figure 1 presents the AWaRe-SAC framework applied to a segment of a mmWave mesh network in a metropolitan city. To evaluate our approach under realistic conditions, we leverage two datasets collected in this metropolitan city: (i) high-frequency link measurements (58–70 GHz) from the mmWave mesh network capture weather-induced attenuation effects; and (ii) residential traffic traces from 943 units across 28 buildings reveal demand patterns and node-level behaviors such as peak usage times and data consumption trends. Combining these datasets enable us to emulate fluctuating link capacity and traffic demand in wireless networks, guiding the design and evaluation of AWaRe-SAC. Our contributions include:

- **Proactive Slice Admission:** We address the unique challenges of slice admission control under link capacity uncertainty with AWaRe-SAC, an end-to-end framework customized to our problem setting that tightly couples deep forecasting of future link capacity levels with predictive Q-learning control.
- **Extensive Real-World Evaluation:** We validate AWaRe-SAC on unique, real-world datasets from a dense urban environment, comprising V-band mmWave links and residential traffic. Our evaluation demonstrates a 15–20% improvement in prediction accuracy and a 2–3x increase in revenue over conventional methods, and our datasets and implementation

will be released for reproducibility.

II. RELATED WORK

Slice Admission Control. Most relevant to AWaRe-SAC is prior work on slice admission using reinforcement learning (RL): [7] modeled the admission control problem as a Semi-Markov Decision Process and solved it with tabular Q-learning. [8]–[10] addressed the problem with deep Q-learning, which uses a deep neural network to represent Q functions, to improve computation efficiency. [11] designed a multi-agent deep RL algorithm, and [12] used an online RL algorithm, SARSA. AI-assisted slice management encompasses a wide range of techniques [13], including max-min optimization for prioritized resource reservation [14], genetic algorithms [15], complex network theory [16], safe slice management using Bayesian optimization [17], risk-averse learning for resource allocation [18], and adaptive orchestration for dynamic O-RAN environments [19]. Most prior work, including the aforementioned studies, *assume static network resources*, whereas real-world x-haul networks are highly sensitive to weather-induced attenuation, which can render existing solutions inadequate for emerging mmWave networks. **Our novel framework not only aims to "pack" as many slices as possible in the available resources, but also minimizes the risk of future penalty.** Introducing time-varying network resources and penalties, unique to our mmWave x-haul scenario, significantly changes both the constraints and the objective of the admission control problem.

Forecasting network resources and traffic demand. Prior work on forecasting traffic demand has evolved from statistical models (e.g., Holt-Winters, ARIMA) to data-driven methods (e.g., LSTM), often assuming static network resources and using simulated slices [20]–[23]. More recently, deep learning frameworks have focused on forecasting network traffic demands to optimize operational cost and QoS [24], [25]. Prior work on forecasting network resources, specifically rain-induced attenuation, used time-series models, including statistical approaches like ARIMA [26] and learning-based methods such as Recurrent Neural Networks (RNNs) [27]–[29]. A comparison of these approaches can be found in [30], [31]. These predictions often support ISAC-related applications, including weather-sensing tasks such as nowcasting [32], [33] and communication-oriented tasks such as rain mitigation [27], [31]. A few works leveraged predictions of the expected network capacity to optimize backhaul routing [34], [35]. Our novel framework predicts the *probability distribution of capacities at future time steps*, which provides information not only about the central tendency but also about the *uncertainty* of the predictions, enabling our slice admission control to minimize penalties incurred from potential future resource underprovisioning.

III. DATASET AND PROBLEM SETTING

A. mmWave Network Measurements

The mmWave mesh network is a community-driven wireless network that provides high-speed internet to residents. While

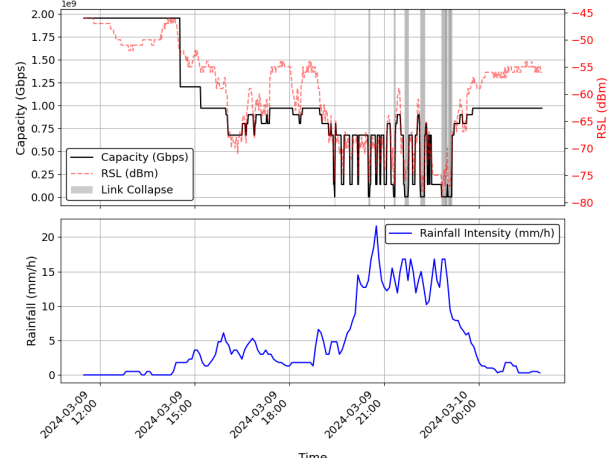


Fig. 2: RSL measurements and rainfall intensities, showing rain-induced attenuation and corresponding capacity levels. the entire network includes hundreds of links, this work focuses on high-frequency links operating in the V-Band up to 70 GHz. These links provide high-capacity and reliable wireless backhaul connections but are also highly sensitive to precipitation along their path.

Dataset Specifications. Our dataset consists of measurements from V-band wireless links operating at carrier frequencies of 58–70 GHz, spanning distances from a few hundred meters to nearly 7 km, and providing gigabit-level capacities for point-to-point and point-to-multipoint connections. Specifically, we collected data from Ubiquiti radio systems, including airFiber 60 LR ('af60') for point-to-point links (up to 1.95 Gbps) and Wave AP ('wave') for point-to-multipoint links, delivering backbone capacities up to 1 Gbps. These measurements allow detailed analysis of weather-induced performance variations in realistic urban network deployments.

Raw Measurements. In this paper, we focus on two key parameters: capacity and Received Signal Level (RSL). Capacity, measured in gigabits per second (Gbps), represents the maximum data rate supported by a link. The RSL collected from the mmWave mesh network links represent the received power at the receiver, quantized in 1 dBm increments and sampled at one-minute intervals. We utilize measurements collected from November 2023 to April 2024, during the winter season in the metropolitan city, encompassing various forms of precipitation such as rain and snow, which contributes to weather-induced signal attenuation. For reference, we also collected weather data from weather stations in the region.

Weather-Induced Capacity Variations. mmWave frequencies (including 60 and 70 GHz bands) are highly sensitive to precipitation, with rain-induced attenuation as one of the primary operational challenges. Rain and other precipitation forms (snow, sleet, fog) cause significant absorption and scattering of mmWave signals, substantially reducing link capacity, reliability, and performance [36], [37]. Fig. 2 shows the measured rainfall alongside RSL and capacity for a 69 GHz mmWave mesh network link (March, 09–10, 2024). During wet periods, attenuation exceeding 30,dB causes link collapses (zero capacity), whereas dry periods maintain stable RSL. To

manage RSL variations and map them to discrete capacity levels, networks often employ a hysteresis-based coding and modulation scheme [38], which we adapt in this work to align with the actual capacity ranges.

B. Network Slice Modeling From User Requests

In the 5G slicing setting, *users* are served by tenants for various service usage. *Tenants* group user demands and request network resources as slices from infrastructure providers. *Infrastructure providers*, in turn, deploy slice admission control algorithms to decide whether to accept or reject incoming slice requests (SRs). Prior work primarily evaluated slicing admission control algorithms on synthetic slices created from simulations or predefined distributions (e.g., Poisson processes) [7], [8], [11], [12], [15], [16], [20], [22]. But, synthetic data does not reflect real user demands, making it hard to evaluate the algorithm's performance in practice. Moreover, standardized protocols for slice creation have not yet been established in the industry. To address the problem, we collect user traces from residential units and create slices from them to develop and evaluate AWaRe-SAC.

Trace Collection. We collect traffic from 520 residential units in off-campus residential buildings. These residential buildings accommodate graduate students, postdocs, and faculty and their families. We anonymize privacy-sensitive fields and discard personally identifiable information.

Associating Network Traces with Services. We group packets with the same 5-tuple (i.e., source IP, destination IP, source port, destination port, transport protocol) as a flow. For each flow between a client and a remote server, we associate the most recent DNS lookup from the client that resolves to the server IP address with each flow. Based on the mapped DNS domains, TLS Server Name Indications (SNI), port numbers, and IP addresses, we associate the flows with specific services.

Slice Generation. We select network traffic for services that fit with the concept of 5G slicing, including Ultra-Reliable and Low Latency Communications (URLLC), Enhanced Mobile Broadband (eMBB), and Massive Machine-Type Communications (mMTC). We filter traffic as follows:

- 1) The eMBB service is designed for high-speed, high-capacity data transmission. We emulate eMBB slices using flows from video streaming and gaming services, including YouTube, Netflix, HBO, Hulu, Steam, and PlayStation.
- 2) The URLLC service is designed for ultra-reliable, low-latency communication services for autonomous vehicles, remote surgery, and so on. We select flows for video conferencing and chatting applications, including Zoom, Snapchat, WhatsApp, and GoogleMessages, to emulate URLL slices.
- 3) The mMTC service caters to the connectivity needs of numerous IoT devices. We cannot identify similar traffic types to emulate it. We envision that IoT devices will generate such traffic.

Then we created slices from the selected flows. A slice is defined by service type, reward, penalty, duration, and throughput requirement. A tenant shall determine reward and

penalty based on service type. We assume that, for management simplicity, a tenant can only provide limited types of slices, meaning a fixed set of throughput and duration options for slices. To use reasonable duration, we calculate the 90th percentile of flow durations within each slicing service category category as the standard duration for that category. All slices requested in that category are then standardized to this duration. To determine reasonable throughput, we compute the 25th, 50th, 75th, and 95th percentiles of aggregated throughput for flows with the same start time and duration. The required throughputs for all SRs in our measurement are 0.4, 8.8, 19.2, and 27.2 Mbps, with 12 slice types in total.

With the above principles, we iterate flows in chronological order and generate the slices as follows: For each incoming flow, if the request can be accommodated with the available capacity and remaining duration of an existing slice, the existing slice will serve the request. Otherwise, a new slice is requested using the request's rounded-up throughput. Since tenants cannot predict flow durations, they may over-request throughput or have flows end early. To optimize resource use, tenants will attempt to fit new flows into existing slices when possible. Additionally, if a flow lasts longer than the SR, the tenant treats the remaining flow as a new flow.

Limitations. While our slices reflect real user demands, we acknowledge that future demands may shift with the rise of autonomous driving and IoT. Nevertheless, we believe leveraging real user data is valuable for designing slice admission control algorithms and hope our work serves as a first step in this direction.

IV. PROBLEM FORMULATION

In this section, we formulate the problem of real-time slice admission control in mmWave networks with time-varying link capacities. Our goal is to design an adaptive admission control strategy that accounts for both predicted capacity changes and time-varying service demands, while balancing rewards and penalties over time. We assume a star-like topology for high-frequency millimeter networks, as shown in Fig. 1. In this model, the infrastructure provider manages the central base station, while tenants operate the edge base stations. Each tenant aggregates user requests at its associated edge base station and forwards SRs to the central base station, where the infrastructure provider makes the admission decisions. The mmWave link capacity fluctuates over time, potentially dropping to zero during severe rain fading events (Fig. 2). Such fluctuations can degrade throughput or cause link collapse, leading to dropped slices. This contrasts with prior work, which assumes constant link capacity for admission control.

Perfect-information MILP formulation. We introduce an Mixed-Integer Linear Programming (MILP) formulation under the assumption of perfect future knowledge of slice arrivals and capacity changes. The MILP formulation is related to the Multidimensional Knapsack problem, with two fundamental differences, i) the Knapsack capacity (i.e., the link) evolves with time, and ii) items (i.e., slices) can be fractionally packed (i.e., underprovisioned) by paying a penalty. The MILP model

must decide not only on which slices to admit, but also how to distribute the channel capacity over time optimally. With reference to the notations in Table I, we express the MILP formulation for the admission control problem as in (1)-(6):

$$\min \sum_{t=1}^H \sum_{i=1}^N P_{it} - \sum_{i=1}^N z_i R_i \quad (1)$$

$$\text{s.t. } z_i = 1 \rightarrow P_{it} \geq a_{ik}(1 - f_{it}) + b_{ik} \quad \forall i \in \{1, \dots, N\}, k \in \{1, \dots, m_i\} \quad (2)$$

$$\sum_{i=1}^N k_{it} d_i f_{it} \leq \text{Cap}_t, \quad \forall i \in \{1, \dots, N\}, t \in \{1, \dots, H\} \quad (3)$$

$$P_{it} > 0 \rightarrow z_{i'} = 0 \quad \forall i \in \{1, \dots, N\}, t \in \{1, \dots, H\}, i' \in \{i \mid t_i = t\} \quad (4)$$

$$f_{it} \in [0, 1], z_i \in \{0, 1\}, P_{it} \geq 0 \quad (5)$$

$$f_{it} \in [0, 1], z_i \in \{0, 1\}, P_{it} \geq 0 \quad (6)$$

Objective function (1) computes the difference between total rewards and penalties. Rewards are lump-sum values gained when slices are accepted. Reward function R_i is given by:

$$R_i = \begin{cases} 0, & z_i = 0 \\ d_i t \rho_i, & z_i = 1 \end{cases}$$

where ρ_i is the price per throughput per time unit paid by a network slice. In contrast, penalties are accumulated for every time slot in which slices are underprovisioned. Specifically, we model the penalty function for underprovisioning as a convex piecewise-linear function, where the argument is the fraction of the total requested throughput allocated to each slice. The function's coefficients depend on the slice type, allowing us to model generic monotonic penalty functions with respect to the degree of overprovisioning. Constraints (2) compute the penalties for admitted slices via an epigraph reformulation of the piece-wise convex linear penalty functions. Constraints (3) are capacity constraints. Constraints (5) prevent admitting new slices in time slots where penalties are greater than zero. In other words, we impose that new slices cannot be admitted whenever there are any underprovisioned slices, which ensures that we prioritize restoring underprovisioned slices. Finally, Constraints (6) define the domains of the decision variables.

Although the MILP formulation cannot be directly applied in practice due to its assumption of perfect information, it guides the design of our real-time algorithm and provides an optimal baseline for benchmarking our adaptive methods. Next, we develop an online admission control framework that leverages real-world network measurements and predictive models to inform its admission control.

V. SYSTEM DESIGN

AWaRe-SAC is a real-time framework that forecasts weather-driven capacity fluctuations and adapts slice admis-

TABLE I: Parameters and decision variables of the perfect-information MILP model.

Parameters & Variables	
N	Number of SRs.
H	Time horizon.
R_i	Reward of admitting slice $i \in \{1, \dots, N\}$.
d_i	Throughput requested by slice $i \in \{1, \dots, N\}$.
t_i	Starting time of slice $i \in \{1, \dots, N\}$.
k_{it}	1 if slice $i \in \{1, \dots, N\}$ is active at time slot $t \in \{1, \dots, H\}$, 0 otherwise.
m_i	Number of intervals in the convex piece-wise linear penalty function for slice $i \in \{1, \dots, N\}$.
a_{ij}, b_{ij}	Coefficient and intercept of the j -th linear segment, $j \in \{1, \dots, m_i\}$, of the penalty function of slice $i \in \{1, \dots, N\}$.
z_i	1 if slice $i \in \{1, \dots, N\}$ is admitted at any time slot, 0 otherwise.
f_{it}	Fraction of requested throughput assigned to slice $i \in \{1, \dots, N\}$ at time slot $t \in \{1, \dots, H\}$.
P_{it}	Penalty incurred by slice $i \in \{1, \dots, N\}$ at time slot $t \in \{1, \dots, H\}$.

sion accordingly. It integrates an AttIRNN predictor (§V-A) with a two-tier admission controller (§V-B).

System Workflow. (1) Historical RSL data is fed into a unified AttIRNN trained across all links. (2) The model outputs per-link capacity distributions over a short horizon. (3) Forecasts and current demands inform admission decisions: a short-horizon MILP computes near-optimal allocations, while Q-learning updates policies under predicted constraints. (4) The controller enforces actions, and new measurements update forecasts in real time.

A. Capacity Predictions with AttIRNN

We first train AttIRNN, an Attention-Integrated RNN to forecast multi-step attenuation power levels with uncertainty over a 5-minute horizon. These predictions are then mapped to expected capacity levels, enabling proactive admission decisions under weather-driven fluctuations.

1) *Prediction Problem Statement:* For each horizon step $t + h$ the model outputs a mean $\hat{\mu}_{t+h}$ and variance $\hat{\sigma}_{t+h}^2$:

$$F_H : \tilde{\mathbf{X}}_t^{(T)} \longmapsto \hat{\mathbf{Y}}_t^{(H)}, \quad \Theta^* = \arg \max_{\Theta} p(\mathbf{Y}_t^{(H)} \mid \tilde{\mathbf{X}}_t^{(T)}; \Theta), \quad (7)$$

where $\hat{\mathbf{Y}}_t^{(H)} = F_H(\tilde{\mathbf{X}}_t^{(T)})$ denotes the predicted sequence, and $\mathbf{Y}_t^{(H)}$ is the true target. The model is trained by maximizing the likelihood of the observed sequence under the predicted parameters at each future step $t + h$.

Here, $\tilde{\mathbf{X}}_t^{(T)}$ is consists of the last- T samples, $\mathbf{X}_t^{(T)} = \{x_{t-T+1}, \dots, x_t\}$, representing the dynamic input, alongside static link specifications $\mathbf{x}_s \in \mathbb{R}^S$ such as carrier frequency, path length, and antenna type that govern rain-attenuation susceptibility [36]. This design allows the model to learn both link-specific behaviors and generalized patterns across a large dataset spanning diverse links.

2) *AttIRNN Model:* AttIRNN is a sequence-to-sequence (Seq2Seq) architecture, illustrated in Fig. 3, that combines

encoder–decoder processing to capture temporal dynamics and static link features through attention mechanism.

Forecasting Setup Each training pair uses the last T RSL inputs, $\mathbf{X}_t^{(T)}$, and the next H future values, $\mathbf{Y}_t^{(H)}$, forming a sliding input–output window pair of length T and H . We denote these generically as $\mathbf{X}_T = \{x_1, \dots, x_T\} \in \mathbb{R}^T$ and $\mathbf{Y}_H = \{y_1, \dots, y_H\} \in \mathbb{R}^H$. This framing converts each time series into a supervised learning problem, where the model learns to predict each future step with $y_h = x_{T+h}$, using $\hat{y}_h = (\hat{\mu}_h, \hat{\sigma}_h^2)$ to represent its expected value and uncertainty within the prediction window.

Encoder–Decoder RNN. A Seq2Seq model [39] maps the input window \mathbf{X}_T to the predicted output sequence $\hat{\mathbf{Y}}_H$ by first encoding the temporal input using a recurrent neural network (RNN). The encoder produces a sequence of hidden states $\phi_1^{(E)}, \dots, \phi_T^{(E)}$, which summarize the input window. The decoder then generates the output sequence $\{\hat{y}_1, \dots, \hat{y}_H\}$ step-by-step, using attention over the encoder states $\phi_j^{(E)}$, the static link embedding \mathbf{g}_s , and its own past hidden states $\phi_{h-1}^{(D)}$.

Static Embedding Branch. AttIRNN leverages static link attributes $\mathbf{x}_s \in \mathbb{R}^S$ to enable cross-link knowledge transfer, capturing rain-attenuation effects across diverse links while preserving the integrity of each time series segment. These static features are embedded into a learned vector $\mathbf{g}_s = \mathbf{W}_s \mathbf{x}_s + \mathbf{b}_s$, which provides a condensed learned representation of link-specific properties for subsequent integration into the model’s later layers.

Integrated Temporal Attention. Attention mechanisms [40], [41] enable neural networks to selectively focus on specific parts of the input, enhancing model performance by computing alignment scores. We use temporal attention to capture time-dependent patterns by aligning each decoder state $\phi_h^{(D)}$ with encoder states $\{\phi_j^{(E)}\}$, enabling dynamic context adaptation instead of relying on the fixed encoder state. This is achieved by computing the alignment scores κ_{hj} and normalizing them into attention weights γ_{hj} :

$$\kappa_{hj} = \mathbf{v}_a^\top \tanh(\mathbf{W}_a[\phi_h^{(D)}; \mathbf{g}_s; \phi_j^{(E)}] + \mathbf{b}_a), \quad (8)$$

$$\gamma_{hj} = \frac{\exp(\kappa_{hj})}{\sum_{k=1}^T \exp(\kappa_{hk})}, \quad (9)$$

Alignment scores κ_{ij} are obtained by transforming the concatenation of $\phi_h^{(D)}$, $\phi_j^{(E)}$, and \mathbf{g}_s via an affine layer ($\mathbf{W}_a, \mathbf{b}_a$) and $\tanh(\cdot)$, then projecting with \mathbf{v}_a^\top . This process yields attention weights γ_{hj} that quantify each encoder hidden state’s contribution to the current decoder step, integrating both temporal and static contexts:

$$\mathbf{g}_h = \sum_{j=1}^T \gamma_{hj} \phi_j^{(E)}, \quad \tilde{\mathbf{g}}_h = [\mathbf{g}_h; \mathbf{g}_s], \quad (10)$$

Here, \mathbf{g}_h summarizes the encoder states $\{\phi_j^{(E)}\}$ via attention weights γ_{hj} , while appending \mathbf{g}_s provides static link-specific context for the prediction phase.

Decoder Probabilistic Predictions The attention mechanism allows the decoder to dynamically attend to encoder states,

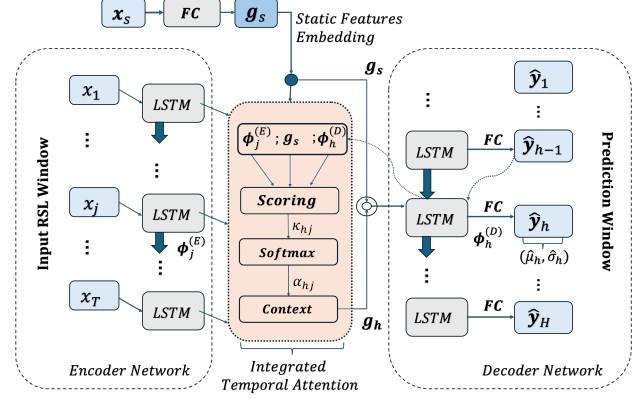


Fig. 3: AttIRNN. Seq2Seq-based predictions with temporal attention for H -step prediction using T -step history.

providing relevant context. The decoder hidden state $\phi_h^{(D)}$ and the output \hat{y}_h are updated as follows:

$$\phi_h^{(D)} = \text{LSTM}(\hat{y}_h, [\phi_{h-1}^{(D)}; \tilde{\mathbf{g}}_h]), \quad (11a)$$

$$\hat{y}_h = \mathbf{W}_o[\phi_h^{(D)}; \tilde{\mathbf{g}}_h] + \mathbf{b}_o. \quad (11b)$$

where \hat{y}_h the previous output, $\phi_{h-1}^{(D)}$ the previous hidden state, and $\tilde{\mathbf{g}}_h$ the enriched context vector combining temporal and static features. \mathbf{W}_o and \mathbf{b}_o are the output layer parameters. The autoregressive decoder structure ensures each \hat{y}_h depends on the enriched context $\tilde{\mathbf{g}}_h$ and previous predictions.

Learning Objective. The negative log-likelihood loss is derived under the assumption that the prediction error $\varepsilon_h = y_h - \hat{\mu}_h$ follows a Gaussian distribution, i.e., $\varepsilon_h \sim \mathcal{N}(0, \hat{\sigma}_h^2)$. Accordingly, the model is trained to maximize the likelihood of the output sequence \mathbf{Y}_H , conditioned on the input window ($\mathbf{X}_T, \mathbf{x}_s$), with the decoder operating autoregressively over past predictions: $p(y_1, \dots, y_H \mid \mathbf{X}_T, \mathbf{x}_s) = \prod_{h=1}^H p(y_h \mid \tilde{\mathbf{g}}_h, y_1, \dots, y_{h-1})$. The loss is computed over all sliding input–output pairs ($\mathbf{X}_T, \mathbf{Y}_H$) in the training data:

$$-\log L(\theta) = \frac{1}{2} \sum_t \sum_{h=1}^H \left[\frac{(y_h - \hat{\mu}_h)^2}{\hat{\sigma}_h^2} + \log \hat{\sigma}_h^2 \right]. \quad (12)$$

This approach learns a Gaussian distribution from which each future value is sampled rather than predicted deterministically, thereby capturing both central tendency (i.e., mean $\hat{\mu}_h$) and uncertainty (i.e., $\hat{\sigma}_h$) associated with future values.

3) Discrete Probability Distribution over Capacity Levels: Each capacity level C_l ($l = 0, \dots, L-1$) has a fixed hysteresis pair $(C_l^\downarrow, C_l^\uparrow)$, where C_l^\downarrow and C_l^\uparrow are the lower and upper RSL thresholds for level C_l , respectively [38]. During inference at time t , given a Gaussian RSL forecast at horizon h , $\hat{y}_{t+h} \sim \mathcal{N}(\hat{\mu}_{t+h}, \hat{\sigma}_{t+h}^2)$, the one-step transition probability from the current level C_k to any level C_l is therefore:

$$\tilde{p}_h(k \rightarrow l) = \Phi\left(\frac{\max(C_l^\uparrow, C_k^\downarrow) - \hat{\mu}_{t+h}}{\hat{\sigma}_{t+h}}\right) - \Phi\left(\frac{\min(C_l^\downarrow, C_k^\uparrow) - \hat{\mu}_{t+h}}{\hat{\sigma}_{t+h}}\right) \quad (13)$$

where $\Phi(\cdot)$ is the standard normal CDF. The min / max operations set the appropriate RSL thresholds, capturing all

hysteresis transitions ("stay," "upward," "downward"). By convention, $C_0^{\downarrow} = -\infty$, with $C_0 = 0$ corresponds to link collapse, and $C_{L-1}^{\uparrow} = +\infty$ indicates nominal capacity.

Assuming a first-order Markov process, the horizon- h probabilities are computed recursively as

$$\tilde{p}_{l,h} = \sum_{k=0}^{L-1} \tilde{p}_h(k \rightarrow l) \tilde{p}_{k,h-1}, \quad h = 2, \dots, H. \quad (14)$$

At each horizon h , the recursion yields a discrete probability vector $\tilde{\mathbf{p}}_{t+h}$, whose elements $\tilde{p}_{l,h}$ represent the estimated likelihood of the link operating at capacity level C_l . This transforms the Gaussian RSL forecast into structured discrete predictions for proactive admission control.

B. Slice Admission Control

1) *Rate Control*: In a dynamic network environment, link capacity may drop below the total required throughput of all slices in the system. To handle this, we underprovision slices in a way that minimizes the overall penalty. To prioritize admitted slices, whenever underprovision occurs, the system stops admitting new slices until the existing slices have recovered their requested throughput. We achieve this goal by solving the following linear program:

$$\min \sum_{i=1}^N P_i \quad (15)$$

$$\text{s.t. } P_i \geq a_{ik}(1 - f_i) + b_{ik}, \quad \forall i \in \{1, \dots, n\}, k \in \{1, \dots, m_i\} \quad (16)$$

$$\sum_{i \in S} d_i f_i \leq \text{Cap}, \quad \forall i \in \{1, \dots, n\} \quad (17)$$

$$f_i \in [0, 1], \quad P_i \geq 0, \quad \forall i \in \{1, \dots, n\} \quad (18)$$

To prioritize admitted slices, whenever underprovision occurs, the system stops admitting new slices until the existing slices have recovered their requested throughput. By iteratively solving the linear program, we dynamically adjust slice allocations to minimize penalties during periods of reduced capacity. This rate control mechanism is integrated into both the Locally Optimal and Predictive Q-learning algorithms described next.

2) *Locally Optimal*: We propose the Locally Optimal algorithm, which leverages predictive capacity to admit slices that maximize the net utility calculated as the total reward from admitted slices minus any penalties incurred from resource underprovisioning. This algorithm does not require prior knowledge of future SRs and solves a variation of the MILP model (1)–(6). The model considers: (1) the batch of incoming slices, each eligible for admission and rate control; (2) admitted slices that require rate control if capacity drops; and (3) a probability vector representing predictive capacity levels over the next five-minute interval. The future capacity scenarios are a discrete set of potential future capacity levels, each associated with a probability derived from analyzing historical fluctuations and AttIRNN.

The Locally Optimal algorithm independently solves the MILP model for each of these predicted capacity scenarios. Subsequently, it calculates the expected net utility by

Algorithm 1 Predictive Q-Learning for Admission Control

```

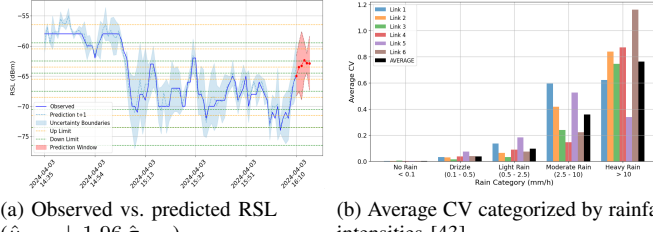
1: Initialize Q-value function  $Q(s, a) = 0, \forall s \in S, a \in A$ 
2: Initialize exploration parameters  $\epsilon, \text{decay\_rate}, \text{min\_epsilon}$ 
3: Initialize occurrence counts  $o(s, a) = 0, \forall (s, a)$ 
4: for each time step  $t$  do
5:   Update current state  $s_t$  based on events at time  $t$ 
6:   If capacity drops below current allocations, Rate Control, otherwise Continue
7:   if there are arriving slices at time  $t$  then
8:     for each arriving slice  $i$  at time  $t$  do
9:       Define action space  $A = \{0, 1\}$  (reject or admit slice  $i$ )
10:      Observe current state  $s_t$ 
11:      Compute predicted future capacity violations  $c_f$  in next 5 minutes
12:      Use  $\epsilon$ -greedy policy to select action  $a_t$ 
13:      Execute action  $a_t$  and Observe immediate reward  $r$ 
14:      Compute penalty $_t = \left(1 - \frac{c_f}{5}\right) \cdot \text{reward} \cdot \text{penalty coefficient}$ 
15:      Observe next state  $s_{t+1}$ 
16:      Increment occurrence count  $o(s_t, a_t) \leftarrow o(s_t, a_t) + 1$ 
17:      Update learning rate  $\alpha_t = \frac{0.5}{o(s_t, a_t)}$ 
18:      Update Q-value  $Q(s_t, a_t)$  using (19)
19:      Set  $s_t \leftarrow s_{t+1}$ 
20: Decay exploration rate:  $\epsilon \leftarrow \max(\epsilon \times \text{decay\_rate}, \text{min\_epsilon})$ 

```

taking a weighted sum of the optimal utilities across all capacity scenarios, using the scenario probabilities as weights: Expected Net Utility = $\sum_i P(C_i) \cdot U(C_i)$, where $P(C_i)$ is the probability of capacity scenario C_i , and $U(C_i)$ the optimal net utility under scenario C_i . This algorithm admits slices that yield the highest expected utility from the current batch of incoming requests. While it makes optimal decisions based on current conditions and predicted capacity, it remains unaware of future SRs. The algorithm potentially admit low-reward slices that blocks the admission of higher-reward slices in the future and its decisions turn out to be suboptimal. The next proposed methodology directly addresses this shortcoming by incorporating longer-term predictions of future SRs.

3) *Predictive Q-Learning*: Predictive Q-Learning extends standard Q-learning [42] by incorporating future capacity predictions, enabling the agent to adapt to both current and anticipated network conditions. It maintains a Q-table $Q(s, a)$ estimating the expected cumulative reward, factoring in future resource availability. At each time step t , the agent observes its current state s_t and the predicted capacity, selects an action a_t based on its current Q-table, and then update $Q(s, a)$ by observing the immediate reward r , the next state s_{t+1} and a predictive penalty factor derived from future capacity indicators. This predictive penalty factor ensures that admission decisions are robust against future resource shortages. Through iterative updates, the algorithm converges to the optimal policy $Q^*(s, a)$, maximizing long-term average net utility.

In Predictive Q-Learning, the state s_t at time t is represented as $s = (\mathbf{n}, \mathbf{R}_{\text{new}}, c_f)$, where $\mathbf{n} = (n_1, n_2, \dots)$ indicates the number of admitted slices by type, \mathbf{R}_{new} represents the arrival of a specific type of SR, and c_f is the predictive indicator of future capacity constraints. c_f denotes the number of future time slots (within a 5-minute window) expected to remain free of capacity violations if the current slice is admitted. Thus, $\left(1 - \frac{c_f}{5}\right)$ quantifies the fraction of time likely to incur overload. The penalty is computed as the product of the slice's reward and a predefined penalty coefficient, scaling with the expected severity of future violations. This penalty explicitly accounts for the predictive consequences of



(a) Observed vs. predicted RSL

$(\hat{u}_{t+1} \pm 1.96 \hat{\sigma}_{t+1})$

(b) Average CV categorized by rainfall intensities [43]

Fig. 4: Time-series RSL prediction with uncertainty bounds and capacity thresholds during rainfall, alongside CV trends grouped by rainfall intensity.

the current admission decision on future capacity constraints, distinguishing our formulation from standard Q-learning. The immediate reward $r(s_t, a_t)$ is obtained by taking action a_t at state s_t . The Q-function is updated iteratively as follows:

$$Q_{t+1}(s_t, a_t) = Q_t(s_t, a_t) + \alpha_t [r(s_t, a_t) - \text{penalty}_t + \max_{a' \in A} Q_t(s_{t+1}, a') - Q_t(s_t, a_t)]. \quad (19)$$

where:

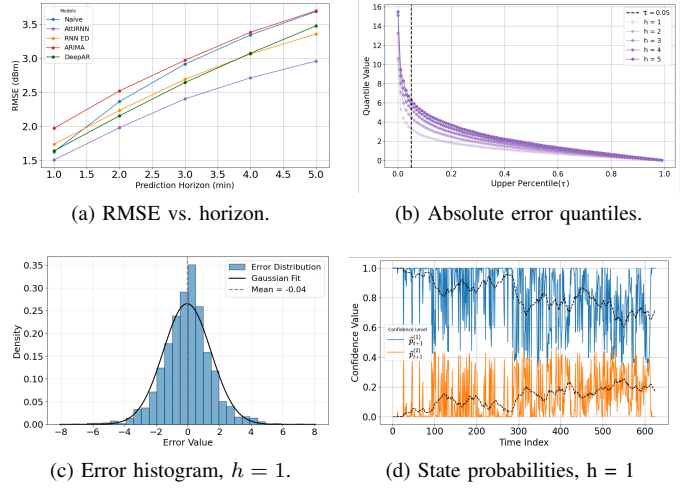
- α_t is the learning rate at time t , determined by the occurrence count $o(s_t, a_t)$ of the state-action pair (s_t, a_t) .
- penalty_t is the penalty factor to discourage actions that lead to future capacity overloads and computed as $(1 - \frac{c_f}{5}) \cdot \text{reward} \cdot \text{penalty coefficient}$

The occurrence count $o(s_t, a_t)$ represents how many times the agent has taken action a_t in state s_t . The learning rate α_t is updated as $\alpha_t = \frac{0.5}{o(s_t, a_t)}$. This choice of α_t ensures that the learning rate decreases over time as the agent becomes more experienced with the state-action pair, which is crucial for the convergence of the Q-learning algorithm. In practice, the agent selects actions using an ϵ -greedy policy, which introduces a parameter ϵ to balance exploration and exploitation. Specifically, with probability ϵ , the agent chooses a random action (exploration), and with probability $1 - \epsilon$, it selects the action that maximizes the current Q-value (exploitation). The discount factor is set to 1 to maximize long-term utility. The exploration rate ϵ decays over time to reduce exploration as the agent becomes more knowledgeable about the environment. The Predictive Q-Learning proceeds as in Algorithm 1.

By incorporating the penalty factor into the Q-value updates, the agent learns to avoid actions that may lead to future capacity overloads, thus optimizing long-term network performance. The iterative process allows the agent to adjust its policy based on observed rewards and penalties, converging to the optimal policy after sufficient iterations. Upon convergence, the algorithm learns a policy that selects the best possible action for each state based on the learned Q-values, maximizing the expected cumulative reward.

VI. EVALUATION

We evaluate our predictor and admission-control policy on real-world data from six V-band links. The **dataset covers 34 h** during three rain events in Mar–Apr 2024:



(a) RMSE vs. horizon.

(b) Absolute error quantiles.

(c) Error histogram, $h = 1$.

(d) State probabilities, $h = 1$

Fig. 5: AttIRNN prediction performance

- **Event I** (9 Mar, 03:15–13:45): mean 5.45 mm/h, peak 21.6 mm/h, duration 10.5 h;
- **Event II** (23 Mar, 02:00–19:00): mean 5.96 mm/h, peak 27.4 mm/h, duration 17 h;
- **Event III** (3 Apr, 10:00–16:00): mean 5.80 mm/h, peak 45.7 mm/h, duration 6 h.

Fig. 4a demonstrates the prediction procedure, showing AttIRNN's one-step forecasts (blue) versus the measured RSL for Link 1 during a rain-event interval. The shaded band marks the 95 % predictive interval, and the dashed lines denote the up- and down-thresholds that separate capacity states.

Temporal fluctuations are quantified via the coefficient of variation ($CV = \sigma/\mu$) of the signal level, a stable proxy for link capacity. Although the raw fluctuations vary with link-specific characteristics and rainfall intensity, CV gives a normalised, uniform metric that lets us evaluate our algorithm's performance across all links and conditions.

Fig. 4b presents the hourly CV for all evaluated links, grouped by rainfall categories [43]. As rainfall intensifies, CV increases sharply, whereas dry periods exhibit near-zero CV, signalling stable capacity.

A. Prediction Evaluation

1) *Baselines*: The **Naive** approach predicts $\hat{x}_{t+h} = x_t$, a simple method that often works well in noisy or volatile conditions. We also use an ARIMA model, a common time-series forecasting method, implemented via auto-ARIMA for automatic parameter tuning [44]. The RNN encoder-decoder model, a widely used Seq2Seq architecture [39], is also a baseline for multi-step predictions. **DeepAR** [45] is an LSTM-based forecasting model that captures complex patterns and uses static features for tailored predictions.

2) *Implementation*: The hyperparameters of the learning models include the lookback window size T , the hidden-layer dimensions, and the temporal attention dimensions. These parameters are optimized on a validation set, with training conducted via the Adam optimizer [46]. All models were

TABLE II: Prediction Performance across CV and horizon.

CV Range	Step	Naive		DeepAR		AttIRNN		
		RMSE	$q_{.95}$	RMSE	$q_{.95}$	RMSE	$q_{.95}$	$\hat{\sigma}$
< 0.25	t+1	0.38	1.09	0.47	1.23	0.40	1.03	0.23 0.96
	t+3	0.65	1.39	0.69	1.39	0.65	1.34	0.30 0.93
	t+5	1.68	1.80	0.80	1.70	0.72	1.56	0.49 0.91
[0.25, 0.75]	t+1	2.89	5.60	2.50	4.62	2.24	4.07	1.35 0.90
	t+3	4.76	8.00	3.95	7.20	3.60	6.48	1.60 0.84
	t+5	5.59	11.50	5.10	10.40	4.94	9.85	1.82 0.79
> 0.75	t+1	3.54	7.91	3.22	7.42	2.41	6.95	2.50 0.87
	t+3	5.75	13.54	4.89	12.89	4.10	11.50	2.94 0.82
	t+5	6.52	17.14	5.56	15.60	5.20	13.55	3.25 0.72

trained and evaluated on NVIDIA GeForce RTX 2080 Ti via PyTorch. The training phase encompassed four months of data (01 November 2023 to 01 March 2024) from the RSL measurements of 25 links. Once trained, the model generates real-time predictions at t , leveraging the learned parameters based on only recent measurements.

3) *Performance of Prediction Models*: Fig. 5 shows the performance of the prediction models. For prediction horizon h , RMSE is defined as $\text{RMSE}_h = \sqrt{\frac{1}{N} \sum_t (x_{t+h} - \hat{x}_{t+h})^2}$, $\forall t$ associated with the evaluation period.

Fig. 5a presents the average RMSE across all links. The proposed AttIRNN consistently yields the lowest errors, showing superior performance in predicting rain-induced attenuation. The Naive model performs comparably at $h = 1$ but exceeds 3.5 dB at $h = 5$, while neural network-based models better capture the attenuation patterns.

Figure 5b plots AttIRNN's absolute prediction errors across all horizons. The 95th-percentile error is about 2.5 dB at $h = 1$ and rises to roughly 7.5 dB for longer horizons, meaning 95 % of errors stay below these levels. Fig. 5c shows the one-step error histogram, centered at zero and well-approximated by a Gaussian distribution. Fig. 5d plots the two largest components of \tilde{p}_{t+1} denoted $\tilde{p}_{t+1}^{(1)}$ and $\tilde{p}_{t+1}^{(2)}$, illustrating how prediction confidence evolves throughout the rain event.

Table II aggregates results over the entire evaluation period, grouping them into three CV bands (low, medium, high) and three horizons ($h = 1, 3, 5$). It also reports AttIRNN's confidence metrics $\hat{\sigma}_{t+h}$ and the mean $\tilde{p}^{(1)}$. When link variability is low ($\text{CV} < 0.25$), all models perform similarly; but at medium ($0.25 \leq \text{CV} < 0.75$) and especially high variability ($\text{CV} \geq 0.75$), AttIRNN has a clear advantage, achieving the lowest RMSE and sharply reduced 95th-percentile absolute errors, indicating both higher accuracy and a lower frequency of significant prediction errors.

B. Admission Control Algorithms Evaluation

We evaluate the performance of the proposed admission control algorithms via simulation. The evaluation is conducted using a dynamic simulation of realistic link capacity and diverse slice characteristics derived from the provided datasets.

1) *Comparative Approaches*: We compare the proposed Predictive Q-learning, with two greedy heuristics, the Locally Optimal algorithm, a naive Q-learning framework, and an offline oracle model (described in §IV). All methods use the same reward/penalty function for fairness.

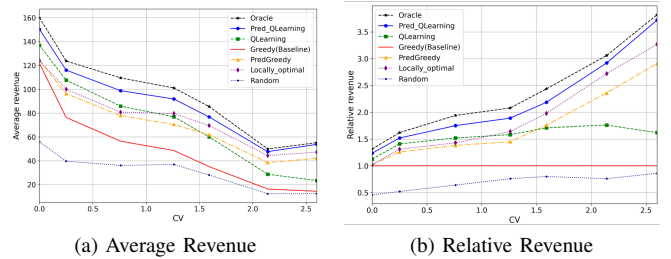


Fig. 6: Revenue comparison under different policies.

The *Naive Greedy* (Baseline) accepts SRs whenever capacity allows, risking resource exhaustion and QoS degradation. The *Predictive Greedy* approach enhances decision-making by incorporating predictions of future capacity. Incoming SRs are ranked based on their reward. The system then sequentially evaluates each incoming. If admitting the SR results in an increase in predicted performance, the SR is accepted; otherwise, the admission process stops at current SR. This approach attempts to balance current utilization with potential future penalties. The *Locally Optimal* approach (described in V-B2) considers both admitted slices and the arriving batch. By solving a MILP, the system makes the best decision for the current batch of incoming SRs without considering future high value SRs. *Naive Q-learning*. [7] proposes a naive Q-Learning framework with the assumption of static capacity and fixed reward for all slices, which does not consider the penalty of underprovisioning the slices when link capacity drops. **Simulation Setup.** We consider 12 classes of slices described in III-B. The average reward of a slice per time slot is the product of its throughput and reward coefficient. In our simulation, the reward coefficient is 1, 5 and 10. We set the penalty coefficient as 2 and the penalty per time slot is then represented as $P(\text{reward}, f_i)$, where p is the penalty function and f_i is the fraction of requested throughput of a slice. The setup considers six sublinks with different CV. Time steps are set to one minute, with capacity predictions derived from AttIRNN extending to the next five minutes.

2) *Simulation Results: Impact of Link variation*. Fig. 6a shows the average reward per admission control model under varying link CVs. A random policy that randomly admits and rejects every SR is included for comparative purposes. As expected, higher variation leads to lower rewards due to more rejections and penalties. Compared to the naive greedy and random baselines (6b), predictive models achieve significantly higher rewards. The naive greedy strategy, ignoring capacity variation, performs nearly as poorly as random admission, while Q-learning without prediction also struggles to adapt to capacity variation. The predictive greedy algorithm improves by leveraging forecasts but still underperforms the Locally Optimal strategy, suggesting that simply incorporating predictions is insufficient without intelligent admission decisions. The proposed predictive Q-learning consistently outperforms others, nearing the offline oracle's performance as CV increases, by dynamically optimizing admissions using predictions.

To highlight the benefit of predictive decision-making from

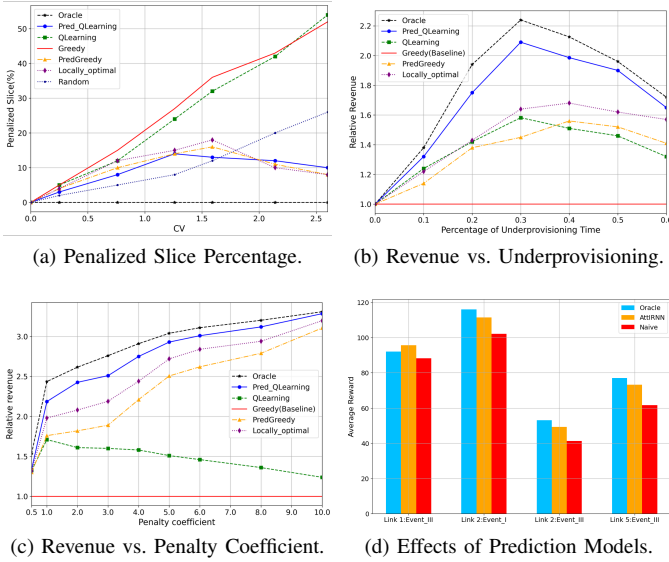


Fig. 7: Revenue analysis under various link conditions.

a network capacity perspective, Fig. 7a shows the proportion of admitted slices whose penalties exceed their rewards. Naive Greedy and Q-learning suffer rising penalty rates under higher link variability due to their inability to anticipate future capacity drops. In contrast, predictive methods, especially Predictive Q-learning, maintain significantly lower penalty rates, demonstrating that foresight reduces costly admission errors and improves resource utilization.

Impact of Underprovisioning Percentage. An environment is defined by link capacity and arriving SRs. We consider an admission control model that unconditionally admits all SRs. The environment is characterized by the percentage of time the system performs rate control on slices admitted under this admit-all policy. A low underprovisioning rate indicates sufficient resources; a high rate signals overload. As shown in Fig. 7b, when the percentage of underprovision is low, all policies can admit all SRs and achieve similar rewards. However, when this percentage is between 0.2 and 0.4, (i.e., the operator has moderate resource availability), the predictive Q-learning algorithm greatly outperforms others by making better admission decisions. For high underprovisioning rates, where resources are extremely scarce, all algorithms degrade due to limited capacity and frequent rate control.

Impact of Penalty Coefficient. Fig. 7c shows the impact of varying the penalty coefficient on the performance of different algorithms and the relative revenue of each model as the penalty for underprovisioning increases. The differences in performance between the predictive models decreases with higher penalties coefficient. When the penalty coefficient grows, all predictive models tend to be conservative and reject all slices that could possibly introduce penalty. In this case, their decisions are highly similar and so are the revenue. Both the naive greedy and Q-learning without prediction strategies perform poorly, as they fail to account for future capacity constraints and thus incur substantial penalties.

Impact of Prediction Models. The previous results use the AttIRNN as the prediction model. The Naive model is easy to adopt in a system, assuming $\hat{c}_{t+h} = c_t$, and serves as a baseline; it can even be effective with unpredictable or noisy data. The AttIRNN model is used to represent an actual prediction model, as it has shown to outperform other baseline models. The Oracle is used to evaluate the model with zero prediction error, serving as the ideal predictor benchmark. We evaluate the impact of the three prediction models. Predictive Q-learning is largely robust to model choice due to its training diversity. However, Fig. 7d shows that prediction accuracy significantly impacts Predictive Greedy and Locally Optimal methods. The Naive model tends to overestimate capacity, reducing performance. AttIRNN, though occasionally misestimating, performs close to the Oracle on average, and moderate overestimation may even help in some cases.

The results demonstrate that the proposed Predictive Q-learning approach consistently outperforms other strategies across diverse scenarios, which can be attributed to several key factors: (i) it makes informed admission decisions by predicting future capacity fluctuations to optimize resource utilization; (ii) it adapts dynamically to changing network conditions, maximizing long-term rewards while minimizing penalties; and (iii) it balances the trade-off between immediate revenue and potential higher-value slices.

VII. CONCLUSION

In this work, we introduced AWaRe-SAC, a novel framework for dynamic slice admission and resource management in x-haul mmWave networks. Our approach addresses the critical challenge of capacity reduction caused by weather-induced attenuation, which poses a direct threat to the performance guarantees of admitted network slices. By integrating proactive management with predictive Q-learning-based slice allocation, utilizing signal forecasts from probabilistic models, AWaRe-SAC maximizes revenue and ensures efficient, adaptive resource utilization.

Our evaluations, leveraging realistic mmWave attenuation measurements collected in dense urban V-band scenarios alongside residential traffic profiles, demonstrate substantial improvements in network slicing efficiency and overall system performance under adverse weather. Consequently, AWaRe-SAC provides a resilient, scalable solution, paving the way for significant advancements in adaptive slicing and robust admission control. Future work will extend AWaRe-SAC into a unified framework that jointly optimizes demand and capacity management, incorporating additional operational datasets for application-driven, risk-aware decision-making, and broadening ISAC applicability to diverse service-level requirements.

REFERENCES

- [1] T. S. Rappaport, S. Sun, R. Mayzus, H. Zhao, Y. Azar, K. Wang, G. N. Wong, J. K. Schulz, M. Samimi, and F. Gutierrez, "Millimeter wave mobile communications for 5G cellular: It will work!" *IEEE Access*, vol. 1, pp. 335–349, 2013.
- [2] P. Nagaraj, "Propagation Characteristics of mmWave and Terahertz Frequencies in 6G Systems," *IEEE Trans. Wireless Commun.*, vol. 13, no. 2, pp. 1–18, 2023.

[3] Y. Niu, Y. Li, D. Jin, L. Su, and A. V. Vasilakos, "A survey of millimeter wave communications (mmWave) for 5G: opportunities and challenges," *Wireless Netw.*, vol. 21, pp. 2657–2676, 2015.

[4] H. Messer, A. Zinevich, and P. Alpert, "Environmental monitoring by wireless communication networks," *Science*, vol. 312, no. 5774, p. 713, 2006.

[5] A. Overeem, H. Leijnse, and R. Uijlenhoet, "Two and a half years of country-wide rainfall maps using radio links from commercial cellular telecommunication networks," *Water Resour. Res.*, vol. 52, no. 10, pp. 8039–8065, 2016.

[6] F. Liu, Y. Cui, C. Masouros, J. Xu, T. X. Han, Y. C. Eldar, and S. Buzzi, "Integrated sensing and communications: Toward dual-functional wireless networks for 6G and beyond," *IEEE J. Sel. Areas Commun.*, vol. 40, no. 6, pp. 1728–1767, 2022.

[7] D. Bega, M. Gramaglia, A. Banchs, V. Sciancalepore, K. Samdanis, and X. Costa-Perez, "Optimising 5G infrastructure markets: The business of network slicing," in *Proc. IEEE INFOCOM*, 2017, pp. 1–9.

[8] N. Van Huynh, D. T. Hoang, D. N. Nguyen, and E. Dutkiewicz, "Optimal and fast real-time resource slicing with deep dueling neural networks," *IEEE J. Sel. Areas Commun.*, vol. 37, no. 6, pp. 1455–1470, 2019.

[9] A. Filali, Z. Mlika, S. Cherkaoui, and A. Kobbane, "Dynamic SDN-based radio access network slicing with deep reinforcement learning for URLLC and eMBB services," *IEEE Trans. Netw. Sci. Eng.*, vol. 9, no. 4, pp. 2174–2187, 2022.

[10] Q. Liu, N. Choi, and T. Han, "OnSlicing: Online end-to-end network slicing with reinforcement learning," in *Proc. ACM CoNEXT*, 2021, pp. 141–153.

[11] M. Sulaiman, A. Moayyedi, M. Ahmadi, M. A. Salahuddin, R. Boutaba, and A. Saleh, "Coordinated slicing and admission control using multi-agent deep reinforcement learning," *IEEE Trans. Netw. Serv. Manag.*, vol. 20, no. 2, pp. 1110–1124, 2022.

[12] G. Dandachi, A. De Domenico, D. T. Hoang, and D. Niyato, "An artificial intelligence framework for slice deployment and orchestration in 5G networks," *IEEE Trans. Cogn. Commun. Netw.*, vol. 6, no. 2, pp. 858–871, 2019.

[13] Y. Wu, H.-N. Dai, H. Wang, Z. Xiong, and S. Guo, "A survey of intelligent network slicing management for industrial IoT: Integrated approaches for smart transportation, smart energy, and smart factory," *IEEE Commun. Surv. Tutor.*, vol. 24, no. 2, pp. 1175–1211, 2022.

[14] Q.-T. Luu, S. Kerboeuf, and M. Kieffer, "Admission control and resource reservation for prioritized slice requests with guaranteed SLA under uncertainties," *IEEE Trans. Netw. Serv. Manag.*, vol. 19, no. 3, pp. 3136–3153, 2022.

[15] B. Han, J. Lianghai, and H. D. Schotten, "Slice as an evolutionary service: Genetic optimization for inter-slice resource management in 5G networks," *IEEE Access*, vol. 6, pp. 33 137–33 147, 2018.

[16] W. Guan, X. Wen, L. Wang, Z. Lu, and Y. Shen, "A service-oriented deployment policy of end-to-end network slicing based on complex network theory," *IEEE Access*, vol. 6, pp. 19 691–19 701, 2018.

[17] Q. Liu, N. Choi, and T. Han, "Atlas: automate online service configuration in network slicing," in *Proc. ACM CoNEXT*, 2022, pp. 140–155.

[18] A. A. Gargari, A. Ortiz, M. Pagin, A. Klein, M. Hollick, M. Zorzi, and A. Asadi, "Safehaul: Risk-averse learning for reliable mmWave self-backhauling in 6G networks," in *Proc. IEEE INFOCOM*, 2023, pp. 1–10.

[19] M. Zhao, Y. Zhang, Q. Liu, A. Kak, and N. Choi, "AdaSlicing: Adaptive online network slicing under continual network dynamics in open radio access networks," in *Proc. IEEE INFOCOM*, 2025, pp. 1–10.

[20] C. Guterman, E. Grinshpun, S. Sharma, and G. Zussman, "RAN resource usage prediction for a 5G slice broker," in *Proc. ACM Int. Symp. Mobile Ad Hoc Netw. Comput. (MobiHoc)*, 2019.

[21] D. Niu, Z. Liu, B. Li, and S. Zhao, "Demand forecast and performance prediction in peer-assisted on-demand streaming systems," in *Proc. IEEE INFOCOM*, 2011, pp. 421–425.

[22] V. Sciancalepore, K. Samdanis, X. Costa-Perez, D. Bega, M. Gramaglia, and A. Banchs, "Mobile traffic forecasting for maximizing 5G network slicing resource utilization," in *Proc. IEEE INFOCOM*, 2017, pp. 1–9.

[23] F. Xu, Y. Lin, J. Huang, D. Wu, H. Shi, J. Song, and Y. Li, "Big data driven mobile traffic understanding and forecasting: A time series approach," *IEEE Trans. Serv. Comput.*, vol. 9, no. 5, pp. 796–805, 2016.

[24] D. Bega, M. Gramaglia, M. Fiore, A. Banchs, and X. Costa-Perez, "DeepCog: Cognitive network management in sliced 5G networks with deep learning," in *Proc. IEEE INFOCOM*, 2019, pp. 280–288.

[25] A. Collet, A. Banchs, and M. Fiore, "Lossleap: Learning to predict for intent-based networking," in *Proc. IEEE INFOCOM*, 2022, pp. 2138–2147.

[26] D. P. Patel, M. M. Patel, and D. R. Patel, "Implementation of ARIMA model to predict Rain Attenuation for KU-band 12 Ghz Frequency," *IOSR J. Electron. Commun. Eng.*, vol. 9, no. 1, pp. 83–87, 2014.

[27] M. N. Ahuna, T. J. Afullo, and A. A. Alonge, "Rain attenuation prediction using artificial neural network for dynamic rain fade mitigation," *SAIEE Africa Res. J.*, vol. 110, no. 1, pp. 11–18, 2019.

[28] D. Jacoby, H. Messer, and J. Ostrometzky, "Spatio-temporal model for predicting multivariate weather-induced attenuation in wireless networks," *IEEE Trans. Instrum. Meas.*, 2025.

[29] D. Jacoby, J. Ostrometzky, and H. Messer, "Short-term prediction of the attenuation in a commercial microwave link using LSTM-based RNN," in *Proc. Eur. Signal Process. Conf. (EUSIPCO)*, 2021, pp. 1628–1632.

[30] —, "Model-based vs. data-driven approaches for predicting rain-induced attenuation in commercial microwave links: A comparative empirical study," in *Proc. IEEE Int. Conf. Acoust., Speech Signal Process. (ICASSP)*, 2023, pp. 1–5.

[31] M. A. Samad and D.-Y. Choi, "Learning-assisted rain attenuation prediction models," *Appl. Sci.*, vol. 10, no. 17, p. 6017, 2020.

[32] R. O. Imhoff, A. Overeem, C. C. Brauer, H. Leijnse, A. H. Weerts, and R. Uijlenhoet, "Rainfall nowcasting using commercial microwave links," *Geophys. Res. Lett.*, vol. 47, no. 19, p. e2020GL089365, 2020.

[33] P. Zhang, X. Liu, and M. Zou, "Reconstructing and nowcasting the rainfall field by a CML network," *Earth Space Sci.*, vol. 10, no. 9, p. e2023EA002909, 2023.

[34] I. Kadota, D. Jacoby, H. Messer, G. Zussman, and J. Ostrometzky, "Switching in the rain: Predictive wireless x-haul network reconfiguration," *Proc. ACM Meas. Anal. Comput. Syst.*, vol. 6, no. 3, pp. 1–26, 2022.

[35] F. Yaghoubi, J. Chen, A. Rostami, and L. Wosinska, "Mitigation of Rain Impact on Microwave Backhaul Networks," in *Proc. IEEE Int. Conf. Commun. Workshops (ICC)*, 2016, pp. 134–139.

[36] ITU-R, "Specific Attenuation Model for Rain for use in Prediction Methods (Recommendation ITU-R P.838-3)," International Telecommunication Union, Geneva, Switzerland, Tech. Rep., 2005.

[37] D. Nandi and A. Maitra, "Study of rain attenuation effects for 5G Mm-wave cellular communication in tropical location," *IET Microw. Antennas Propag.*, vol. 12, no. 9, pp. 1504–1507, 2018.

[38] L. Bao, J. Hansryd, T. Danielson, G. Sandin, and U. Noser, "Field trial on adaptive modulation of microwave communication link at 6.8 GHz," in *Proc. Eur. Conf. Antennas Propag. (EuCAP)*, 2015, pp. 1–5.

[39] K. Cho, B. van Merriënboer, C. Gulcehre, D. Bahdanau, F. Bougares, H. Schwenk, and Y. Bengio, "Learning phrase representations using RNN encoder-decoder for statistical machine translation," arXiv preprint arXiv:1406.1078, 2014.

[40] D. Bahdanau, K. Cho, and Y. Bengio, "Neural machine translation by jointly learning to align and translate," arXiv preprint arXiv:1409.0473, 2014.

[41] A. Vaswani, N. Shazeer, N. Parmar, J. Uszkoreit, L. Jones, A. N. Gomez, L. Kaiser, and I. Polosukhin, "Attention is all you need," in *Proc. Adv. Neural Inf. Process. Syst. (NeurIPS)*, 2017.

[42] C. J. C. H. Watkins and P. Dayan, "Q-learning," *Mach. Learn.*, vol. 8, no. 3-4, pp. 279–292, 1992.

[43] World Meteorological Organization, "Manual on Codes: International Codes, Volume I.I, Annex II to the WMO Technical Regulations," World Meteorological Organization (WMO), Geneva, Switzerland, Tech. Rep. WMO-No. 306, 2017.

[44] R. J. Hyndman and Y. Khandakar, "Automatic time series forecasting: the forecast package for R," *J. Stat. Softw.*, vol. 27, pp. 1–22, 2008.

[45] D. Salinas, V. Flunkert, J. Gasthaus, and T. Januschowski, "DeepAR: Probabilistic forecasting with autoregressive recurrent networks," *Int. J. Forecast.*, vol. 36, no. 3, pp. 1181–1191, 2020.

[46] D. P. Kingma and J. Ba, "Adam: A method for stochastic optimization," arXiv preprint arXiv:1412.6980, 2014.